



Regional representation of F2 Chapman parameters based on electron density profiles

M. Limberger¹, W. Liang², M. Schmidt², D. Dettmering², and U. Hugentobler¹

¹Technische Universität München – Institute of Astronomical and Physical Geodesy (IAPG), Arcisstr. 21, 80333 München, Germany

²Deutsches Geodätisches Forschungsinstitut (DGFI), Alfons-Goppel-Str. 11, 80539 München, Germany

Correspondence to: M. Limberger (marco.limberger@bv.tum.de)

Received: 23 August 2013 – Revised: 8 November 2013 – Accepted: 15 November 2013 – Published: 20 December 2013

Abstract. Understanding the physical processes within the ionosphere is a key requirement to improve and extend ionospheric modeling approaches. The determination of meaningful parameters to describe the vertical electron density distribution and how they are influenced by the solar activity is an important topic in ionospheric research. In this regard, the F2 layer of the ionosphere plays a key role as it contains the highest concentration of electrons and ions. In this contribution, the maximum electron density $NmF2$, peak height $hmF2$ and scale height $HF2$ of the F2 layer are determined by employing a model approach for regional applications realized by the combination of endpoint-interpolating polynomial B splines with an adapted physics-motivated Chapman layer. For this purpose, electron density profiles derived from ionospheric GPS radio occultation measurements of the satellite missions FORMOSAT-3/COSMIC, GRACE and CHAMP have been successfully exploited. Profiles contain electron density observations at discrete spots, in contrast to the commonly used integrated total electron content from GNSS, and therefore are highly sensitive to obtaining the required information of the vertical electron density structure. The spatio-temporal availability of profiles is indeed rather sparse, but the model approach meets all requirements to combine observation techniques implicating the mutual support of the measurements concerning accuracy, sensitivity and data resolution. For the model initialization and to bridge observation gaps, the International Reference Ionosphere 2007 is applied. Validations by means of simulations and selected real data scenarios show that this model approach has significant potential and the ability to yield reliable results.

Keywords. Ionosphere (equatorial ionosphere; modeling) – radio science (ionospheric physics)

1 Introduction

The steadily increasing number of appropriate measurements goes hand in hand with the availability of different observation techniques that may contribute individual sensitivities for resolving ionospheric key parameters. The majority of prevailing observation-driven ionosphere models consider the spatial and temporal variations of the total electron content (TEC) derived mainly or even only from GNSS measurements due to the availability of a dense data distribution. A widely used approach is the modeling of TEC variations in terms of a 3-D description with respect to longitude, latitude and time, while the vertical distribution of the electron density (N_e) is mostly not considered. Among other things, this is rooted in the fact that terrestrial GNSS measurements provide the TEC as an integral observable between the emitting satellite and the ground-based receiver, which is rather insensitive for the description of the electron density distribution with respect to height. Electron density profiles derived from radio occultation measurements may be used instead or in combination with other observation types to provide the required support for the determination of key parameters with height dependency. At its inception, the GPS radio occultation technique was tested by means of the Global Positioning System/Meteorology (GPS/MET) experiment, which was carried out between 1995 and 1997 by the University Corporation for Atmospheric Research (UCAR). Based on this pilot experiment, first promising results of limb sounding

of the Earth's atmosphere and ionosphere could be obtained (Ware et al., 1996; Hajj and Romans, 1998). Several low Earth orbiter (LEO) missions were launched afterwards, such as the German Challenging Minisatellite Payload (CHAMP) in July 2000, which was operated by the German Research Centre for Geosciences (GFZ) and ended in September 2010. The tandem satellite mission Gravity Recovery and Climate Experiment (GRACE) was launched in 2002 and is operated by a cooperation of NASA and the German Aerospace Center (DLR). Further improvements concerning the observation coverage have been achieved with the joint US–Taiwanese mission Formosa Satellite 3 and Constellation Observing System for Meteorology, Ionosphere, and Climate (FORMOSAT-3/COSMIC) as a result of the constellation of six satellites on six orbital planes with a 30° separation. The FORMOSAT-3/COSMIC satellites fly in an altitude of approximately 800 km, while for CHAMP and GRACE an initial orbit of around 450–500 km was chosen. All three missions are adequate for sounding the electron density peak region of the ionospheric F2 layer, which is typically located at an altitude of approximately 250–350 km in midlatitudes and under certain conditions up to 500 km in equatorial regions (Hoque and Jakowski, 2012).

The spaceborne atmospheric radio occultation technique allows for tracking of electromagnetic (EM) signals that have been modified by interactions with the atmospheric medium (Kirchengast et al., 2004). The geometry between the source transmitting the EM signal and the receiver is the key to ensure the propagation of the signal in limb-sounding geometry. In the case of GPS radio occultation, a receiver flown on a LEO satellite tracks the phase and amplitude of the GPS signal, while the GPS satellite sets or rises behind the Earth's atmosphere (= setting/rising occultation). The obtained observations contain information on the vertical refractivity below the LEO orbit and therefore enable the extraction of electron density profiles, which can be derived from the ionospheric index of refraction. Retrieval methods have been described in several publications such as Jakowski et al. (2002) or Tsai and Tsai (2004). The derived profiles contain discrete N_e observations that structurally describe the electron density distribution along the measured points. Relevant physical quantities such as the maximum electron density $NmF2$ or the corresponding peak height $hmF2$ become more or less directly visible. However, the data distribution given by retrieved electron density profiles is by far not as dense as for terrestrial GNSS, but the potential of profiles can be exploited in 4-D modeling. The vertical description of the electron density can be approximated by a Chapman function that has been successfully used in several applications for sounding the planetary ionosphere. The original Chapman layer was introduced in the 1960s by Rishbeth and Garriot (1969) for modeling the ionospheric electron density for a fixed atmospheric scale height. Variations of the original functions for an improved description of certain layers have been established over the years; for example, Reinisch et al.

(2007) introduced a modification of the original α -Chapman layer with a continuously varying scale height to model the F2 topside electron density. The model presented in this paper will take an adapted α -Chapman layer into account that was proposed by Jakowski (2005) and considers a F2 ionosphere layer for a fixed scale height plus a slowly decaying plasmasphere term. It can be described by a total of five key parameters where this contribution covers the determination of the F2 layer-related key parameters contained in the α -Chapman layer by means of exclusively electron density profiles. After the introduction of the mathematical and physics-motivated model (Sect. 2), the adjustment system, which forms the backbone of the parameter estimation, will be explained in detail (Sect. 3). The model validation will be carried out in several stages, comprising a closed-loop simulation (Sect. 4.1) and real data analysis (Sect. 4.2) with investigations on the key parameters (Sect. 4.2.1) and also TEC (Sect. 4.2.2).

2 Model

To model the vertical electron density, an adapted α -Chapman layer is introduced to allow for the consideration of the ionospheric F2 layer and the plasmasphere (Jakowski, 2005). It consists of a F2 Chapman function and a slowly decaying exponential term, which allow for a smooth transition between the topside electron density of ionosphere and plasmasphere. The model equation finally yields

$$\begin{aligned}
 N_e(h) &= \underbrace{N_e^{F2}(h, NmF2, hmF2, HF2)}_{\text{F2 layer}} + \underbrace{N_e^P(h, N0P, HP)}_{\text{Plasmasphere}} \\
 &= NmF2 \exp \left[\frac{1}{2} \left(1 - \frac{h - hmF2}{HF2} - \exp \left(\frac{hmF2 - h}{HF2} \right) \right) \right] \\
 &\quad + N0P \exp \left(\frac{-|h - hmF2|}{HP} \right) \quad (1)
 \end{aligned}$$

and contains five descriptive key parameters, namely the maximum electron density of the F2 layer $NmF2$, the corresponding F2 peak height $hmF2$, the F2 topside scale height $HF2$, the plasmasphere basis density $N0P$ and the plasmasphere scale height HP . Following Jakowski (2005), a physically reasonable value of 10^4 km for HP (in the case of $h > hmF2$, otherwise 10 km) and the assumption of proportionality between $N0P$ and $NmF2$ can be taken into account. It should be kept in mind that the F2 scale height differs with respect to bottomside and topside ionosphere but is assumed to be equal in the model approach presented here.

Each of the key parameters can be modeled in terms of three 1-D endpoint-interpolating polynomial B spline functions with regard to longitude λ , latitude φ and time t with initially unknown series coefficients d . The basic theory about B spline modeling is, for example, given by Schumaker (1981) and Lyche and Schumaker (2000), and discussions on the application of B splines to model the regional vertical total electron content (VTEC) have already been published by

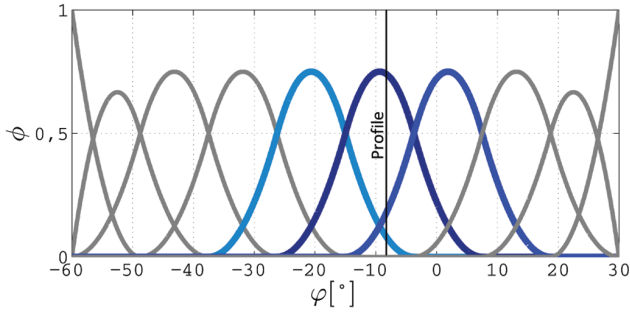


Fig. 1. Endpoint-interpolating polynomial B splines of level $J = 3 \rightarrow K = 10$ within $[-60^\circ, +30^\circ]$ latitude. The blue splines are influenced by the exemplary profile (black line) located at $\varphi = -8^\circ$.

Schmidt (2007), Zeilhofer et al. (2008) and Dettmering et al. (2011a). Polynomial B splines are chosen due to their advantage of the endpoint-interpolating and localizing characteristic for regional modeling, meaning that the spline values are constrained at the boundaries and generally are nonzero just within a compact interval. Results of the comparison between B splines and spherical harmonics and their different advantages with respect to regional and global modeling are given by Schmidt et al. (2011) and will not be further discussed at this point. Each measurement and vertical profile penetrates a certain number of B spline functions and consequently contributes to the determination of the corresponding series coefficients. Figure 1 shows a 1-D representation of endpoint-interpolating polynomial B splines based on level $J = 3$ within an area of $\varphi = [-60^\circ, +30^\circ]$. In the case of one dimension, the function values $f(\varphi)$ are computed from the scaling functions $\phi_k^{J_\varphi}(\varphi)$ by

$$f(\varphi) = \sum_{k=1}^{K(J_\varphi)} d_k^{J_\varphi} \phi_k^{J_\varphi}(\varphi) \quad (2)$$

and $d_k^{J_\varphi}$ are the series coefficients labeled with their affiliation to the corresponding $\phi_k^{J_\varphi}$. $K(J_\varphi)$ denotes the number of B spline functions calculated from

$$K(J_\varphi) = 2^J + 2 \quad (3)$$

according to the associated B spline level J_φ . Consequently $J_\varphi = 3$ defines 10 splines that are distributed over the given latitude sector. The endpoint-interpolating characteristic of polynomial B splines becomes clearly visible at the boundaries where only the first and last two scaling functions are modified. With regard to the use of electron density profiles, a black line has been depicted to indicate an exemplary profile and its influence zone. The profile is located at $\varphi = -8^\circ$ and solely penetrates the blue splines. Accordingly, each electron density observation supports exactly three spline functions in the case of modeling one dimension.

The transfer from one to n dimensions is achieved by the consideration of tensor products composed of n 1-D scaling

functions. Figure 2 shows an example for a 2-D representation based on

$$f(\lambda, \varphi) = \sum_{k_1=1}^{K(J_\lambda)} \sum_{k_2=1}^{K(J_\varphi)} d_{k_1, k_2}^{J_\lambda, J_\varphi} \phi_{k_1}^{J_\lambda}(\lambda) \phi_{k_2}^{J_\varphi}(\varphi), \quad (4)$$

where the situation refers to a two-dimensional scenario regarding latitude φ $[-60^\circ, +30^\circ]$ and longitude λ $[250^\circ, 340^\circ]$. The spline levels are defined as $J_\lambda = 2$ and $J_\varphi = 3$, and therefore the area is covered by $6(\lambda) \times 10(\varphi) = 60$ spline functions. An exemplary profile located at $\lambda = 304^\circ$ and $\varphi = 0^\circ$ is depicted as a solid black line where the cuboid covers all the splines that are located in the intersection zone of profile and splines. In this case, altogether $3(\lambda) \times 3(\varphi) = 9$ splines are affected by a single profile at a specific time. The modeling approach presented in this paper considers time as the third dimension to be modeled by polynomial B splines, and consequently $3(\lambda) \times 3(\varphi) \times 3(t) = 27$ splines are influenced by a single observation at a specific time. In terms of the B spline expression, the description of a specific key parameter yields

$$\kappa_r(\lambda, \varphi, t) = \sum_{k_1=1}^{K(J_\lambda)} \sum_{k_2=1}^{K(J_\varphi)} \sum_{k_3=1}^{K(J_t)} d_{k_1, k_2, k_3}^{J_\lambda, J_\varphi, J_t} \phi_{k_1}^{J_\lambda}(\lambda) \phi_{k_2}^{J_\varphi}(\varphi) \phi_{k_3}^{J_t}(t), \quad (5)$$

where κ_r denotes a specific key parameter identified by the subscript $r \in \{1, \dots, R\}$ with the total number R of key parameters intended to be determined, i.e., in the case of the three F2 Chapman parameters: $\kappa_1 = NmF2$, $\kappa_2 = hmF2$ and $\kappa_3 = HF2$. The unknown target quantities to be determined are B spline series coefficients with respect to each F2 key parameter, which henceforth are substituted with the coefficient vector \mathbf{d} . $K(J) \in \{K(J_\lambda), K(J_\varphi), K(J_t)\}$ and $J \in \{J_\lambda, J_\varphi, J_t\}$ are distinguished with respect to the given dimensions. The higher the level J , the sharper the spline functions and consequently the higher the detail resolution. Accordingly, J should be consistent with the given observation density. Under the assumption of a constant observation sampling Δsi on the interval $[si_{\min}, si_{\max}]$, the relation

$$\Delta si < \frac{si_{\max} - si_{\min}}{K(J) - 1} \quad (6)$$

will be taken into account (Schmidt et al., 2011). Rearrangements and the substitution of $K(J) = 2^J + 2$ based on Eq. (3) lead to

$$J < \log_2 \left(\frac{si_{\max} - si_{\min}}{\Delta si} - 1 \right) \quad (7)$$

and show the dependency between the defined B spline level J and data sampling Δsi . This formulation obviously has been developed for the case of a homogeneous data distribution. Although the distribution of electron density profiles is rather sparse and inhomogeneous, this definition can be used to find rough estimations for suitable B spline levels.

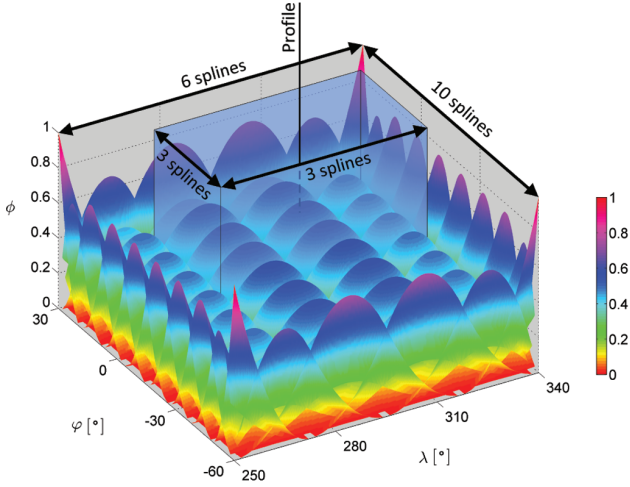


Fig. 2. 2-D B spline representation referring to $\lambda = [250^\circ, 340^\circ]$ and $\varphi = [-60^\circ, 30^\circ]$. The embedded transparent cuboid borders the influence zone of a profile that is indicated by the black solid line. Altogether, $3 \times 3 = 9$ splines are affected.

3 Determination of B spline series coefficients

For the determination of \mathbf{d} a Gauss–Markov model is established (Koch, 1999). A general expression for the functional and stochastic part is respectively given by

$$\mathbf{A}\mathbf{d} = \mathbf{l} + \mathbf{e}_l \quad \text{and} \quad \boldsymbol{\Sigma}_l = \sigma_l^2 \mathbf{P}_l^{-1}. \quad (8)$$

Here, \mathbf{A} is the $n \times u$ coefficient matrix with full column rank, the so-called design matrix, where n is the total number of observations and u is the number of unknowns, i.e., the total number of unknown B spline series coefficients collected in \mathbf{d} . In particular, \mathbf{d} is the $u \times 1$ vector that contains the unknown coefficients referring to the different key parameters $\mathbf{d} = (\mathbf{d}_{\kappa_1}^T, \dots, \mathbf{d}_{\kappa_R}^T)^T$. \mathbf{P}_l is the known positive definite $n \times n$ weight matrix of the observations collected in the $n \times 1$ vector \mathbf{l} and \mathbf{e}_l indicates observation noise. Furthermore, σ_l^2 identifies the unknown variance component of the observations and $\boldsymbol{\Sigma}_l$ is the corresponding $n \times n$ covariance matrix. Since the data distribution of electron density profiles is rather sparse, data gaps have to be bridged by prior information for the unknown series coefficients. The corresponding functional and stochastic model for the prior information can be found with

$$\mathbf{d} = \boldsymbol{\mu} + \mathbf{e}_\mu \quad \text{and} \quad \boldsymbol{\Sigma}_\mu, \quad (9)$$

where $\boldsymbol{\mu}$ indicates the $u \times 1$ vector of prior information with the $u \times u$ covariance matrix $\boldsymbol{\Sigma}_\mu$ and \mathbf{e}_μ denotes the prior information error. $\boldsymbol{\Sigma}_\mu$, in particular, contains the individual unknown variance components $\sigma_\mu^2 \in \{\sigma_{\kappa_1}^2, \sigma_{\kappa_2}^2, \dots, \sigma_{\kappa_R}^2\}$ as well as the known positive definite $u \times u$ weight matrices $\mathbf{P}_\mu \in \{\mathbf{P}_{\kappa_1}, \mathbf{P}_{\kappa_2}, \dots, \mathbf{P}_{\kappa_R}\}$ of the unknown key parameters and thus yields

$$\boldsymbol{\Sigma}_\mu = \text{diag} \left(\sigma_{\kappa_1}^2 \mathbf{P}_{\kappa_1}^{-1}, \sigma_{\kappa_2}^2 \mathbf{P}_{\kappa_2}^{-1}, \dots, \sigma_{\kappa_R}^2 \mathbf{P}_{\kappa_R}^{-1} \right). \quad (10)$$

In this paper, the weighting matrices \mathbf{P}_l and \mathbf{P}_μ for observations and prior information are applied as identity matrices; that is, equal weights without consideration of observation or prior information correlations are introduced. The observation model given by Eq. (1) is highly nonlinear and thus requires a linearization in order to apply the linear model defined on the left of Eq. (8). Therefore a Taylor series expansion based on a first-order approximation is performed. The linearized model for a specific observation i reads

$$N_e(h)_i = N_e(\kappa_1(\mathbf{d}_{\kappa_1,0}), \dots, \kappa_R(\mathbf{d}_{\kappa_R,0}))_i + \sum_{r=1}^R \left(\left[\frac{\partial N_e}{\partial \kappa_r} \right]_0 \left[\frac{\partial \kappa_r}{\partial \mathbf{d}_{\kappa_r}} \right]_0 \right)^T \Delta \mathbf{d}_{\kappa_r}, \quad (11)$$

where each key parameter κ_r is modeled by an appropriate set of corresponding series coefficients \mathbf{d}_{κ_r} according to Eq. (5). Afterwards, the normal equations for a single observation technique can be derived by

$$\left(\frac{1}{\sigma_l^2} \mathbf{A}^T \mathbf{P}_l \mathbf{A} + \mathbf{W} \right) \Delta \hat{\mathbf{d}} = \frac{1}{\sigma_l^2} \mathbf{A}^T \mathbf{P}_l \mathbf{L} + \mathbf{W} \mathbf{M}, \quad (12)$$

where \mathbf{W} substitutes an extended weight matrix with the block diagonal structure

$$\mathbf{W} = \boldsymbol{\Sigma}_\mu^{-1} = \text{diag} \left(\frac{\mathbf{P}_{\kappa_1}}{\sigma_{\kappa_1}^2}, \frac{\mathbf{P}_{\kappa_2}}{\sigma_{\kappa_2}^2}, \dots, \frac{\mathbf{P}_{\kappa_R}}{\sigma_{\kappa_R}^2} \right) \quad (13)$$

containing individual variance factors and weight matrices of the unknown key parameters. The observation vector, originally denoted as \mathbf{l} , is now replaced by the reduced observation vector \mathbf{L} that contains the differences between observed and computed initial electron densities

$$L_i = N_e(h)_i - N_e(\kappa_1(\mathbf{d}_{\kappa_1,0}), \dots, \kappa_R(\mathbf{d}_{\kappa_R,0}))_i \quad (14)$$

resulting from the linearization step in Eq. (11). The hat symbol used for $\Delta \hat{\mathbf{d}}$ symbolizes that the coefficient corrections are outcomes of the adjustment process and are identified as estimated quantities. \mathbf{M} stabilizes the system and counteracts a possible ill-conditioning of the normal equations in the case of data gaps where \mathbf{W} regularizes the proper weighting of the prior information. Since this approach is based on an iterative solving procedure, \mathbf{M} has to be adapted after each iteration step with respect to the linearization by

$$\mathbf{M}_{it} = \boldsymbol{\mu} - \left(\mathbf{d}_0 + \sum_{j=1}^{it} \Delta \hat{\mathbf{d}}_j \right), \quad (15)$$

where “it” denotes a specific iteration. Reliable prior information is inevitably required and can be extracted from a given background model such as the climatologically driven International Reference Ionosphere 2007 (IRI-2007), (Bilitza and Reinisch, 2008). In our paper we derived both the vector

of prior information μ and the initial values d_0 for the series coefficients from IRI-2007, but it should be kept in mind that the data sources for those coefficients that serve as prior and initial information may differ. In the case of $\mu = d_0$ the expression for the final iteration yields

$$M_{IT} = - \sum_{j=1}^{IT} \Delta \hat{d}_j \quad (16)$$

and “IT” substitutes the total number of required iterations until an appropriate threshold for the final solution is exceeded.

3.1 Initial and prior information

Naturally, the linearization introduced by Eq. (11) brings along the requirement for initial values of the unknown parameters. This means specifically that initial series coefficient vectors $d_{k_1,0}, \dots, d_{k_R,0}$ have to be introduced where, in the ideal case, initial values are derived in a preprocessing step from an external model. Additionally, by using electron density profiles exclusively, the observation coverage is rather sparse and leads to the presence of data gaps that have to be bridged by prior information. The basic principles of the prior information model have been explained previously in terms of Eqs. (9) and (15). The selection of a suitable background model for providing prior information is in any case quite important and some trust should be placed in it since the corresponding information is used to overcome data gaps and can only be improved in those regions where observations are given. IRI-2007 is considered here as the only data source used for the derivation of initial and prior information since it complies with the criterion to provide data of all three key parameters where *NmF2* and *hmF2* as well as *VTEC* are directly available. The derivation of initial values and prior information for *HF2* follows from the computation of the slab thickness τ , which is defined as the ratio between *VTEC* and *NmF2*, as introduced by Davies (1990). Moreover, Wright (1960) showed the equality of τ with $4.13 \cdot HF2$ for an α -Chapman layer. This relation is generally accepted and has been adopted in other publications such as Jayachandran et al. (2004). Initial values for *HF2* result from these relations in

$$\tau = \frac{VTEC}{NmF2} = 4.13 \cdot HF2 \rightarrow HF2 = \frac{VTEC}{4.13 \cdot NmF2}. \quad (17)$$

The availability of a suitable background model thus allows for the derivation of initial grid-based key parameters basically without data gaps, and subsequently the determination of initial B spline series coefficients $d_{k_r,0}$ resulting from a general Gauss–Markov least-squares estimation by

$$d_{k_r,0} = (\mathbf{A}_{k_r}^T \mathbf{P}_l^{\text{back}} \mathbf{A}_{k_r})^{-1} \mathbf{A}_{k_r}^T \mathbf{P}_l^{\text{back}} \mathbf{l}_{k_r}^{\text{back}}. \quad (18)$$

$\mathbf{P}_l^{\text{back}}$ is considered as an identity matrix; that is, the same observation weights are considered and no relative weightings

are introduced. \mathbf{A}_{k_r} contains the partial derivatives for the initially unknown coefficients based on Eq. (5) and consequently its entries equal the tensor products of the spline values $\phi_{k_1}^{J_\lambda}(\lambda)\phi_{k_2}^{J_\varphi}(\varphi)\phi_{k_3}^{J_t}(t)$ depending on the defined B spline levels J_λ, J_φ and J_t . Values of the initial key parameters provided by the background model are introduced as observations collected in $\mathbf{l}_{k_r}^{\text{back}}$. It has to be kept in mind that the detail resolution is controlled by the B spline levels, and accordingly the representation of the background model eventually becomes smoothed if the defined levels are low.

3.2 Combination of different observation techniques and missions

In order to account for the combination of various observation techniques, the system of normal equations in consideration of multiple observation groups has to be adapted and yields

$$\left(\sum_{q=1}^Q \frac{1}{\sigma_q^2} \mathbf{A}_q^T \mathbf{P}_q \mathbf{A}_q + \mathbf{W} \right) \Delta \hat{d} = \sum_{q=1}^Q \frac{1}{\sigma_q^2} \mathbf{A}_q^T \mathbf{P}_q \mathbf{L}_q + \mathbf{W} \mathbf{M}, \quad (19)$$

where $q \in \{1, \dots, Q\}$ has been introduced to indicate specific observation techniques. Individual variance components, i.e., weighting factors for all observation techniques σ_q^2 including the prior information $\sigma_{k_r}^2$, are determined by an iterative maximum-likelihood variance component estimation (VCE) to account for the different accuracies. These variance factors are estimated iteratively taking approximate starting values into account. The approach is described in Koch and Kusche (2002) and applied to ionosphere modeling in Dettmering et al. (2011b). Here, the VCE is realized in a similar manner but has been extended to take different groups of unknowns into account. The computation of variance factors then follows from

$$\hat{\sigma}_q^2 = \frac{\hat{\mathbf{e}}_q^T \mathbf{P}_q \hat{\mathbf{e}}_q}{r_q} \quad \text{and} \quad \hat{\sigma}_{k_r}^2 = \frac{\hat{\mathbf{e}}_{k_r}^T \mathbf{P}_{k_r} \hat{\mathbf{e}}_{k_r}}{r_{k_r}} \quad (20)$$

for the different observation techniques and prior information groups, respectively. The vectors of residuals, $\hat{\mathbf{e}}_q$ and $\hat{\mathbf{e}}_{k_r}$, are obtained with

$$\hat{\mathbf{e}}_q = \mathbf{A}_q \Delta \hat{d} - \mathbf{L}_q \quad \text{and} \quad \hat{\mathbf{e}}_{k_r} = \Delta \hat{d}_{k_r} - \mathbf{M}_{k_r}. \quad (21)$$

The partial redundancies, r_q and r_{k_r} , yield

$$r_q = n_q - \text{Tr} \left(\frac{1}{\sigma_q^2} \mathbf{A}_q^T \mathbf{P}_q \mathbf{A}_q \mathbf{N}^{-1} \right) \quad (22)$$

and

$$r_{k_r} = u_{k_r} - \text{Tr} \left(\frac{1}{\sigma_{k_r}^2} \mathbf{P}_{k_r} \mathbf{S}_{k_r} \right), \quad (23)$$

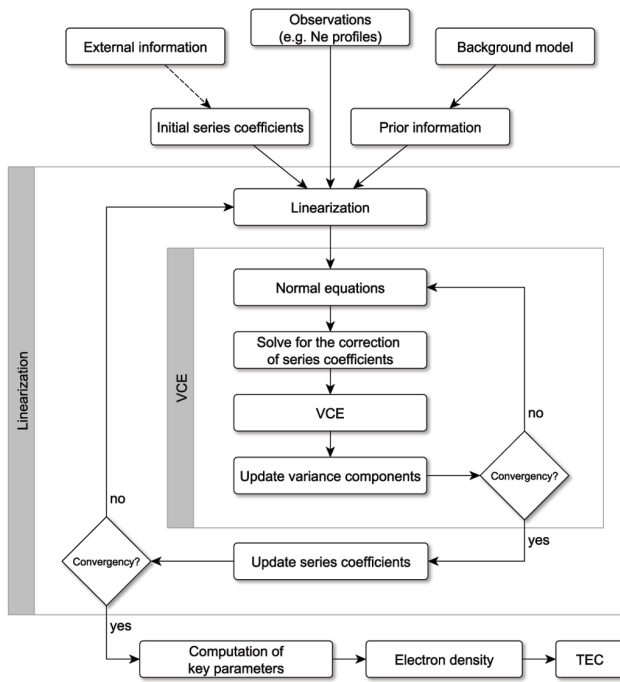


Fig. 3. Flowchart of the main processing steps.

where \mathbf{N} substitutes the $u \times u$ normal equations matrix, i.e., the left-hand side of Eq. (19),

$$\mathbf{N} = \sum_{q=1}^Q \frac{1}{\sigma_q^2} \mathbf{A}_q^T \mathbf{P}_q \mathbf{A}_q + \mathbf{W}, \quad (24)$$

and \mathbf{S}_{κ_r} denotes the key parameter specific submatrices along the diagonal of \mathbf{N}^{-1} . The realization of the described approach for the parameter estimation comprises now two iterations according to the linearization and the VCE implemented as a nested loop that considers the VCE as the inner iteration and the linearization as the outer. A flowchart of the most relevant processing steps is depicted in Fig. 3. After estimating the final sets of series coefficients, key parameters with respect to λ , φ and t may be constructed. Afterwards, the 4-D electron density distribution can be calculated from the adapted Chapman function and even allows for reconstruction of TEC values in consideration of an appropriate integration function. A possible reconstruction sequence hence covers the estimation of B spline series coefficients (Eq. 19) and subsequently the determination of F2 Chapman key parameters (Eq. 5), followed by the computation of the electron density (Eq. 1) and TEC.

4 Numerical investigations

For the study of the modeling approach described above, a selected region covering mainly South America within $\lambda \in [250^\circ, 350^\circ]$ and $\varphi \in [-60^\circ, +30^\circ]$ has been considered. Electron density profiles composed of discrete N_e

observations derived from ionospheric GPS radio occultation are used as the input data. In particular, measurements of the FORMOSAT-3/COSMIC (Taiwan–US), GRACE (US–Germany) and CHAMP (Germany) LEO satellite missions have been taken into account. Mission specifications are provided by the operating organizations and can be found on the corresponding websites at <http://www.cosmic.ucar.edu/>, <http://www.csr.utexas.edu/grace/> and <http://op.gfz-potsdam.de/champ/>. The processing of scientific data for the FORMOSAT-3/COSMIC mission is done by the UCAR. The Center for Space Research (CSR) at the University of Texas at Austin and the GFZ in Potsdam perform the data processing of the GRACE mission. The GFZ was also responsible for the data processing of CHAMP until it was decommissioned. Here we consider preprocessed CHAMP and GRACE electron density profiles kindly provided by the Institute of Communications and Navigation of the DLR and preprocessed FORMOSAT-3/COSMIC data from the Center for Space and Remote Sensing Research (CSRSR) of the National Central University (NCU) in Taiwan. The applied profiles passed different preprocessing strategies. A typical method is the consideration of the Abel inversion technique based on bending-angle data or slant total electron content (STEC) to derive electron density profiles. The assumption of a spherical symmetry in the nearby area during an occultation event is one of the drawbacks considered in the classical Abel transform. To overcome this assumption, improved strategies have been developed. Aragon-Angel (2010) for instance proposes a strategy based on the separability concept, introduced by Hernández-Pajares et al. (2000), where horizontal VTEC gradients are taken into account and the excess phase rate is considered as the main observable. CSRSR provides routinely processed data based on an improved Abel inversion process through compensated TEC values under consideration of horizontal electron density gradients published by Tsai et al. (2009). DLR’s preprocessing strategy follows the concept of a tomographic voxel approach published by Jakowski et al. (2004) and Jakowski (2005).

4.1 Closed-loop simulation

In order to validate our modeling approach, a closed-loop simulation has been carried out in order to assess the ability of the adjustment system to solve for all three F2 Chapman parameters simultaneously.

For the simulation procedure we choose real geographical locations and epochs of the measurements meaning that λ , φ and t are taken from real data, but simulated electron density observations have been considered. A specific measurement is simulated by

$$\tilde{N}_e(h)_i = \left(\tilde{N}_e^{\text{F2}}(h, \tilde{\kappa}_1, \dots, \tilde{\kappa}_R) + N_e^{\text{P}}(h, \text{NOP}, \text{HP}) + \tilde{\epsilon}_q \right)_i \quad (25)$$

with

$$\tilde{\kappa}_r = \kappa_r(\mathbf{d}_{\kappa_r, 0}) + \tilde{C}_{\kappa_r}, \quad (26)$$

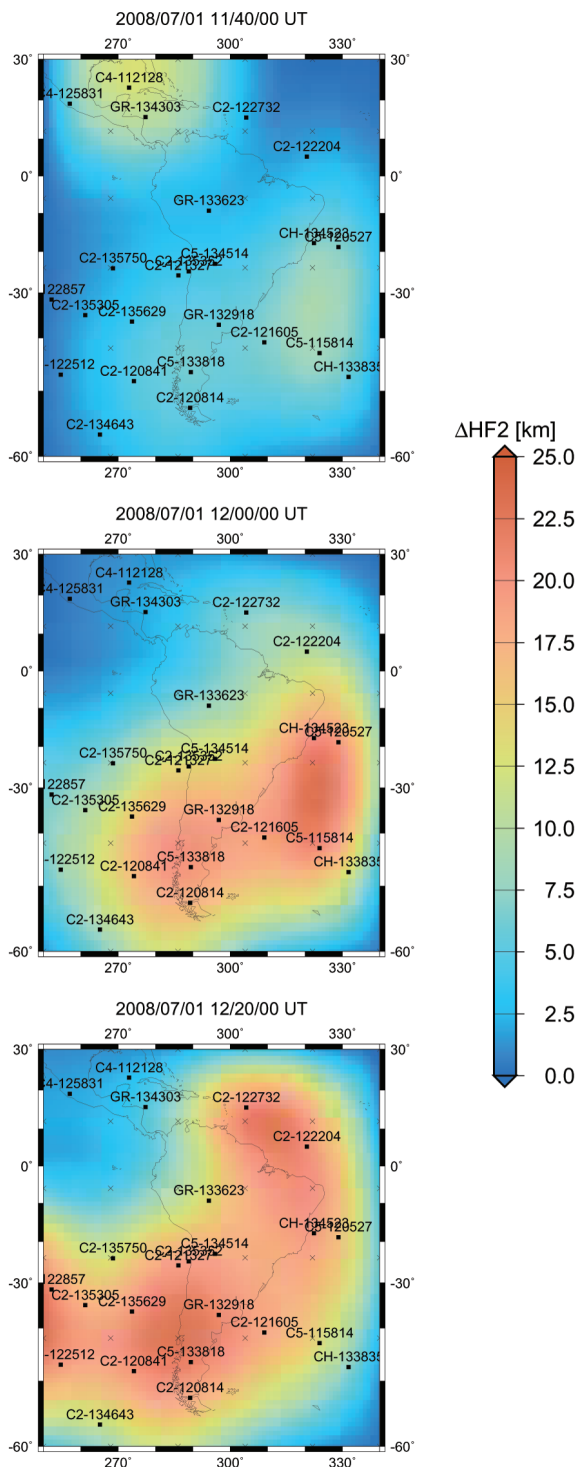


Fig. 4. Estimated scale height corrections $\Delta HF2 = HF2(\hat{d}_{HF2}) - HF2(d_{HF2,0})$ for 1 July 2008 at 11:40 UT (top), 12:00 UT (center) and 12:20 UT (bottom) based on the B spline levels $J_\lambda = 2$, $J_\varphi = 2$ and $J_t = 3$. Each electron density profile is labeled with a corresponding mission identifier: (C)osmic, (CH)amp or (GR)ace and the Universal Time of the observation.

where the tilde symbols indicate simulated quantities and \tilde{C}_{κ_r} are constants to simulate systematic biases referring to the different F2 key parameters. For the computation of $d_{\kappa_r,0}$ the IRI-2007 background model has been taken into account. $\tilde{\epsilon}_q$ is the mission-dependent simulated observation error based on random white noise with expectation value $E(\tilde{\epsilon}_q) = 0$ and standard deviation

$$\sigma_{\tilde{\epsilon}_q} = \left(\frac{0.02}{N_p} \cdot \sum_{p=1}^{N_p} \max(N_{e,p}) \right)_q \quad (27)$$

This implies that 2% of the averaged maximum electron density with respect to each profile $p \in \{1, \dots, N_{p,q}\}$ of a certain satellite mission q is adopted. Within a closed-loop simulation it is then possible to validate the approach in terms of reconstructing the introduced systematic discrepancies by means of the simulated \tilde{N}_e observations. This first validation is based on simulated data covering a time frame of three hours between 11:00 and 14:00 UT at 1 July 2008. In total, 19 FORMOSAT-3/COSMIC profiles (including 4871 discrete N_e observations), 3 GRACE profiles (including 63 N_e observations) and 2 CHAMP profiles (including 48 N_e observations) are taken into account. In the case of using exclusively electron density profiles, the data distribution is rather sparse. Additionally, one has to consider that the N_e profile reconstruction from ionospheric radio occultation implicates assumptions within the preprocessing where each pointwise electron density observation refers to a larger area with a diameter of up to 2000 km. Therefore, relatively low B spline levels of $J_\lambda = 2$, $J_\varphi = 2$ and $J_t = 3$ have been applied. In total, the B spline coverage then includes $6 \times 6 \times 10$ spline functions and hence, under the rough assumption of $1^\circ = 111$ km, there is a spline peak every 2000 km in λ and φ direction and every 20 min. The predefined systematic biases are listed in Table 1 and represent the “true” corrections considered within the simulated observations. The estimated corrections, determined within the closed-loop simulation, are depicted in Fig. 4 as an example of the F2 scale height with

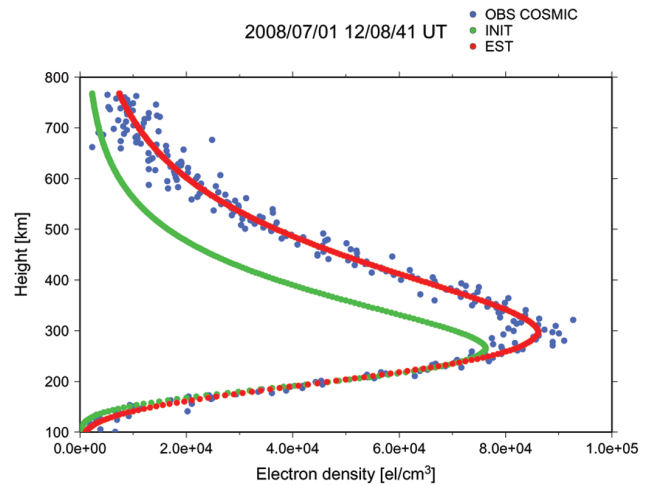
$$\Delta HF2 = HF2(\hat{d}_{HF2}) - HF2(d_{HF2,0}). \quad (28)$$

Consecutive time steps at 11:40, 12:00 and 12:20 UT are illustrated. B spline peaks are depicted as black crosses and profile locations are marked as black squares where the observed profiles are identified by an abbreviation that indicates the corresponding mission (GR = GRACE, CH = CHAMP, Cx = FORMOSAT-3/COSMIC with satellite identification number x) and Universal Time (UT) (e.g., 133818 = 13:38:18 UT). The key parameter maps demonstrate the impact of different profiles with respect to time and location. Corrections appear at those locations and times where measurements are given, while the adapted B spline levels control the degree of smoothing and consequently affect the extent of the correction zones. Due to the low

Table 1. Simulated systematic deviation.

C_{NmF2}	C_{hmF2}	C_{HF2}
10^4 el cm^{-3}	30 km	20 km

B spline levels, a strong smoothing effect is achieved. Blue areas indicate the presence of data gaps and consequently remain uncorrected; that is, the estimated scale height is defined by the prior information and thus shows a systematic deviance of 20 km from the “true” value. Other regions show good agreement between the estimation and the “truth”, indicated by corrections around $\Delta HF2 = 20$ km. The full correction can certainly only be obtained where the observation time of an illustrated profile correlates with the time moment represented by the image. The C2-122204 profile located at $\lambda = 320^\circ$ and $\varphi = 5^\circ$ in the northeast region provides a good example that demonstrates how the measurements influence the estimated correction in correlation with time and position. This profile has been observed around 12:20 UT and consequently shows a steadily increasing influence from 12:00 UT until its strongest impact on the bottom images related to 12:20 UT. The C4-112128 profile located at $\lambda = 273^\circ$, $\varphi = 23^\circ$ close to the northern boundary still has an influence at 11:40 UT, which completely vanishes afterwards. Some regions between profiles show an obvious overestimation of around 5–6 km for $\Delta HF2$. For example, on the 12:20 UT image, clearly visible by the intense red coloring. In these cases, two or more profiles are affecting the estimation of $\Delta \hat{d}_{HF2}$ at the same time. Since all profiles carry the information that the values of the initial parameters need to be increased (due to the simulated homogeneous systematic biases), the estimation procedure adjusts a surface through the measured values at the locations of the profiles and the surrounding a priori values, which causes a peak value between the profile locations. Whether such under- or overestimations are present thus depends on the spatial and temporal distribution of the profiles and on the measured values. To get an impression of the conformity between observed and estimated profiles, Fig. 5 shows the N_e values referring to the initial (green), simulated (blue) and estimated (red) electron density profiles with respect to height as an example for a selected C2 profile observed at 12:08:41 UT and located at $\lambda = 274^\circ$, $\varphi = -48^\circ$. The simulated electron density observations include the artificial input noise, defined by Eq. (27), which has been adapted differently with respect to the LEO missions. The difference between the observations and initial values is caused by the simulated systematic differences of the key parameters where the systematically increased $NmF2$ - and $hmF2$ -related offsets are visible right away and the higher $HF2$ causes an increase in the thickness of the profile. In the case of simulations, model errors do not appear, which allows for the comparison between the standard deviations of the simulated input noise $\sigma_{\hat{\varepsilon}}$ and the

**Fig. 5.** Initial (green), simulated (blue) and estimated (red) electron density values referring to a simulated FORMOSAT-3/COSMIC profile observed at $\lambda = 274^\circ$, $\varphi = -48^\circ$ and 1 July 2008 12:08:41 UT

standard deviations of the outcome residuals $\sigma_{\hat{\varepsilon}_q}$ related to the differences between observed and estimated electron density. Table 2 shows a comparison of $\sigma_{\hat{\varepsilon}_q}$ and $\sigma_{\hat{\varepsilon}_q}$ in relation to the considered LEO missions. The standard deviations of the residuals fit well together with the input noise levels and indicate a successful retrieval of the key parameters by the simulated electron density observations. Following Eq. (27), the noise is computed from the mean of the maximum electron densities of all profiles per mission. Therefore the magnitude of the input noise can naturally differ depending on whether the majority of profiles are located in regions with higher electron density (e.g., inside the crest region) or in quiet areas. The previous investigations were focused on the example of $HF2$ but also hold for $NmF2$ and $hmF2$. For the simulations, $HF2$ has been chosen as it is the most nonlinear and therefore weakest parameter in the system located in the denominator of the (twofold) exponential term; see Eq. (1).

4.2 Real data

The model assessment has been successfully carried out by means of simulated electron density data. In the next step, real data of FORMOSAT-3/COSMIC, GRACE and CHAMP are considered to obtain first results for the time frame between 11:00 and 14:00 UT on 1 July 2008. The year 2008 is characterized by low solar conditions and therefore offers a suitable basis for the evaluation of the modeling approach with real data. Again, B spline levels of $J_\lambda = 2$, $J_\varphi = 2$ and $J_r = 3$ have been accepted. In contrast to the closed-loop simulation, unusable profiles are removed here within a data-screening procedure to guarantee that the electron density structure around the peak can be described properly. Therefore, only profiles covering at least an altitude range of

Table 2. Standard deviations of simulated input noise and observation residuals.

	FORMOSAT-3/ COSMIC			CHAMP	GRACE
$\sigma_{\hat{\epsilon}_q}$ [el cm ⁻³]	3387.6	8541.5	7371.2		
$\sigma_{\hat{e}_q}$ [el cm ⁻³]	3384.2	7924.8	7215.7		

$hmF2 \pm 50$ km are considered where the detected $hmF2$ value of a specific profile must be located within an altitude region between 150 and 450 km as several erroneous profiles were found to show multiple electron density peaks in physically unrealistic altitudes. Other profiles are dominated by noise and have been eliminated. Figure 6 shows two examples related to a suitable electron density profile and to a profile that was detected as an outlier. The first profile clearly shows the peak region of the F2 layer and is only weakly influenced by lower layers such as the E region. The second profile shows large noise above 500 km, indicating data problems. From this profile, a reliable determination of $hmF2$ is not possible and thus it is rejected. Table 3 gives an overview on the data-screening statistics. The total number of available electron density profiles is reduced from 28 to 17 suitable profiles. In particular, the number of FORMOSAT-3/COSMIC profiles has been depleted from 22 to 12, while only 1 CHAMP profile has been rejected and all GRACE profiles remain. Accordingly, altogether 39 % of the electron density profiles, mainly disturbed by high noise, are detected as outliers and have been rejected.

4.2.1 Key parameter evaluation

The representation of the F2 key parameters as a function of λ , φ and t based on the estimated B spline series coefficients is described by Eq. (5). It is important to note that the reconstruction does not depend on discrete grid points. The desired key parameters can be reconstructed at any location and time, while the detail resolution is controlled by the defined B spline levels. The spatial variations of the reconstructed key parameters for a specific epoch are depicted in Fig. 7 with a resolution of $\Delta\lambda = \Delta\varphi = 2.5^\circ$ and $\Delta t = 6$ min. In the left column the estimated corrections of the estimated key parameters $\kappa_r(\hat{\mathbf{d}})$ to the initial values $\kappa_r(\mathbf{d}_0)$ are shown for 12:00 UT, where

$$\Delta hmF2 = hmF2(\hat{\mathbf{d}}_{hmF2}) - hmF2(\mathbf{d}_{hmF2,0}),$$

$$\Delta HF2 = HF2(\hat{\mathbf{d}}_{HF2}) - HF2(\mathbf{d}_{HF2,0}),$$

and

$$\Delta NmF2 = NmF2(\hat{\mathbf{d}}_{NmF2}) - NmF2(\mathbf{d}_{NmF2,0}).$$

The colorbars are adapted to the minimum and maximum correction for the selected epoch. Again, key parameters are only corrected in areas where profiles support the estimation

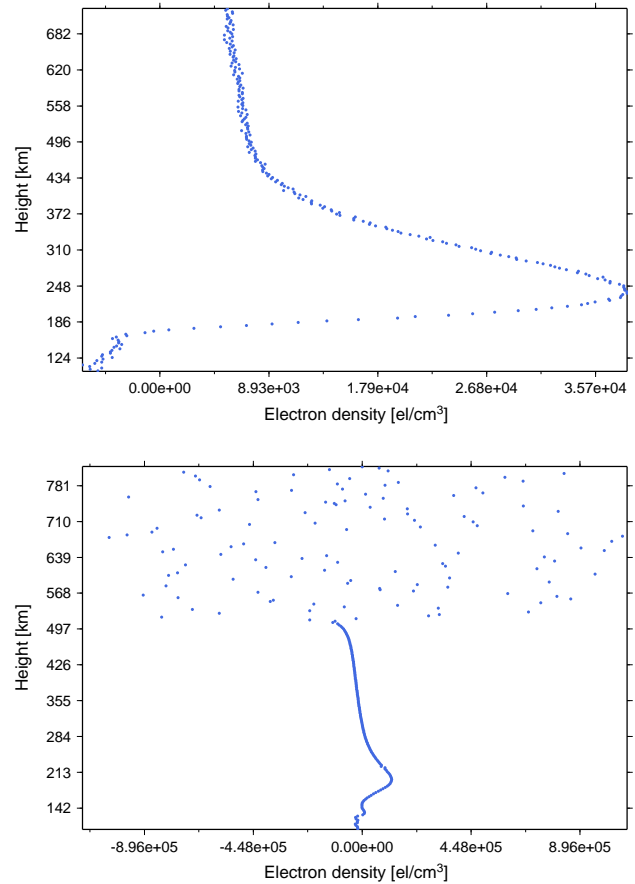


Fig. 6. Examples for a suitable (top) and an unusable (bottom) electron density profile observed by FORMOSAT-3/COSMIC

of the corresponding coefficients. Three selected profiles that have a strong impact on the estimated corrections are given along the right column, where observations (blue), initial values (green) and estimated values (red) are illustrated. These profiles are indicated by arrows on the key parameter correction maps. The image on top shows a profile that was observed at $\lambda = 289^\circ$, $\varphi = -52^\circ$ and mainly affects $hmF2$. Apart from that, $NmF2$ experiences a decrease, which becomes visible in the corresponding $\Delta NmF2$ correction map. The changes with respect to $HF2$ are clearly explainable by the middle profile, located at $\lambda = 286^\circ$ and $\varphi = -25^\circ$, where the observed curve, and consequently the estimated curve, is more narrow than the initial profile. The bottom profile is located at $\lambda = 320^\circ$, $\varphi = 5^\circ$ and obviously has a strong influence on the $NmF2$ estimation but also causes a slight decrease of $hmF2$. In particular, $NmF2$ is reduced by almost 2×10^5 el cm⁻³, which mainly roots from the impact of a lower atmospheric layer, possibly the E layer. The Chapman profile in this case is not able to approximate the observed profile correctly. Our model thus results in a systematic bias influencing the estimation of the key parameters, a situation that could be improved by rejecting

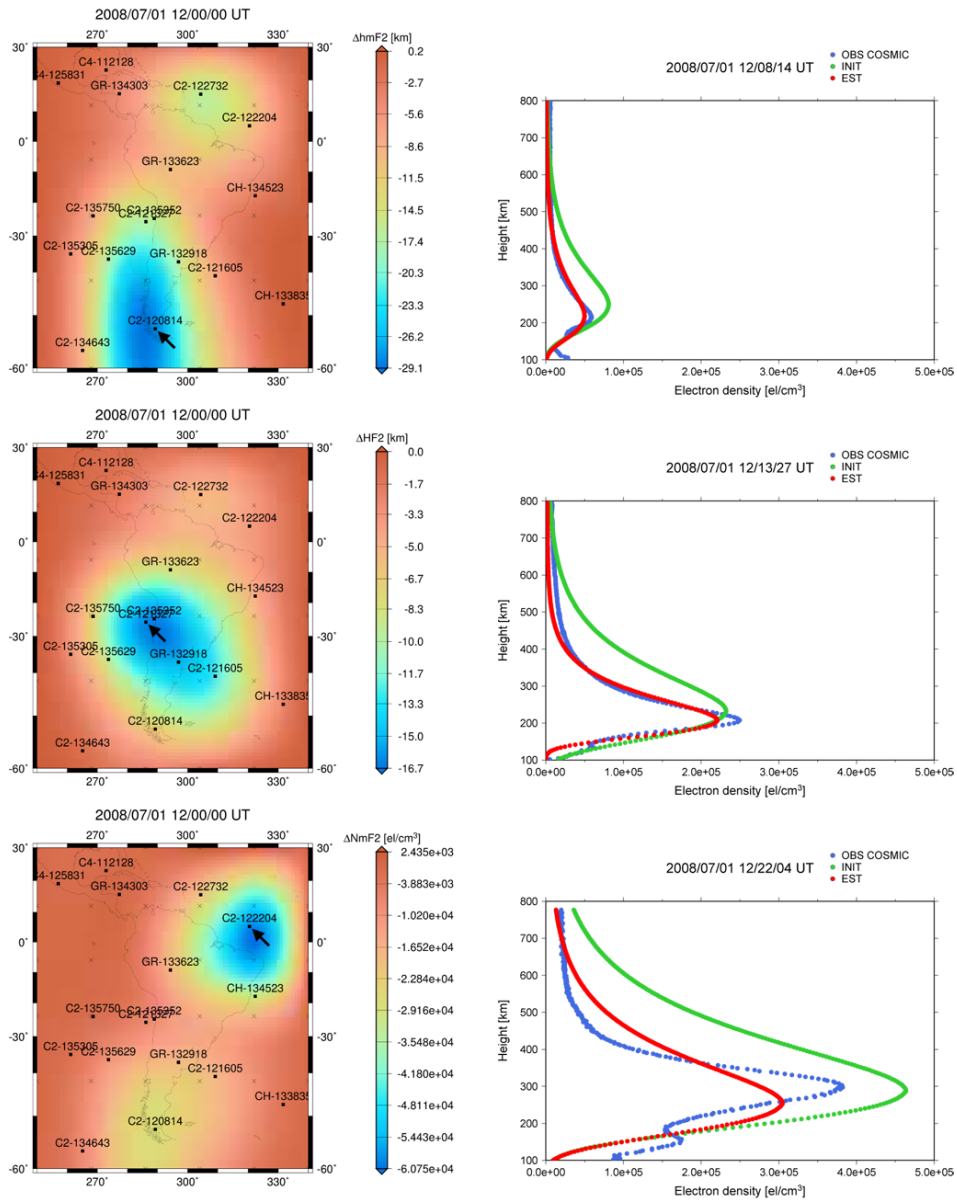


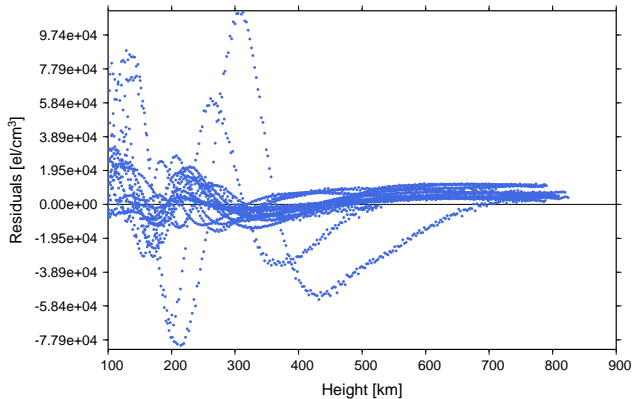
Fig. 7. Key parameter corrections $\Delta NmF2$, $\Delta hmF2$ and $\Delta HF2$ for a fixed time moment at 12:00 UT on 1 July 2008 (left column). Selected FORMOSAT-3/COSMIC profiles that have an impact on the key parameter estimation (right column). These profiles are indicated by arrows on the key parameter maps.

observations at lower atmospheric layers or by implementing an additional E layer into the model. The impact of the mismodeling can be seen in Fig. 8, where the residuals of all FORMOSAT-3/COSMIC profiles observed in the given time period are depicted. The mismodeling effect obviously increases towards lower altitudes and causes an oscillation of the estimated values around the observed values as a function of height. This oscillation effect can be expected from the bottom FORMOSAT-3/COSMIC profile in Fig. 7, where the E layer is very dominant and forces the model to adjust the Chapman layer as a compromise between the F2 and E layer. The estimated red curve consequently swings

around the blue observed curve. The standard deviation of the residuals, taking all FORMOSAT-3/COSMIC observations into account, is $\hat{\sigma}_{\text{COS}} = 18.3 \times 10^3 \text{ el cm}^{-3}$. Standard deviations of the residuals in Fig. 8 separated into two altitude regions, up to 400 km and above 400 km, yield $\hat{\sigma}_{\text{COS}}^{<400} = 24.1 \times 10^3 \text{ el cm}^{-3}$ and $\hat{\sigma}_{\text{COS}}^{\geq 400} = 10.2 \times 10^3 \text{ el cm}^{-3}$, respectively, and support the prediction of larger mismodeling effects in the case of a dominant E layer. In general it can be noticed from Fig. 7 that all three key parameters are decreased with respect to the initial state, which allows for the implication that the IRI-2007 key parameter values are too high for the considered time period.

Table 3. Total, rejected and remaining electron density profiles before and after the data-screening process.

	Total	Rejected	Remaining
FORMOSAT-3/COSMIC	22	10	12
GRACE	3	0	3
CHAMP	3	1	2
Total	28	11	17

**Fig. 8.** Observation residuals related to all FORMOSAT-3/COSMIC electron density profiles observed on 1 July 2008 between 11:00 and 14:00 UT.

4.2.2 VTEC evaluation

In the following, reconstructed VTEC values computed with our model are validated by comparison with IRI-2007 data and global ionosphere maps (GIMs) provided by the International GNSS Service (IGS). Dow et al. (2009) and Hernández-Pajares et al. (2009) published detailed information on the IGS network structure and services including ionospheric products. IGS GIMs are computed with data from the IGS global GNSS tracking network and become publicly available in Ionosphere Map Exchange format (IONEX) with a resolution of 2 h and $\Delta\lambda = 5^\circ \times \Delta\varphi = 2.5^\circ$ in time and space, respectively. As based on observations, IGS GIMs represent a good reference for the validation of our model. In general, VTEC can be computed from

$$\text{VTEC} = \int_{h_{\text{bottom}}}^{h_{\text{top}}} \hat{N}_e(h) dh \quad (29)$$

as an integral of the estimated model electron density along a vertical path through the ionosphere between the altitude limits h_{bottom} and h_{top} with path element dh . The concept for the implemented numerical integration algorithm is described in Zeilhofer et al. (2008), where an integration layer covering the ionosphere with an upper and lower boundary is

defined. Here, an integration layer subdivided into three sublayers with intervals defined by [80 km, 200 km], [200 km, 1200 km] and [1200 km, 2000 km] has been applied. The integration within each of these sublayers is performed with individual integration step sizes to account for different characteristics of the ionospheric layers. Further, each integration step is carried out by means of a Gauss–Legendre quadrature of order N , where $N = 6$ has been found to be adequate as a compromise between accuracy and performance. VTEC maps for IRI-2007, IGS GIM and the difference between IRI-2007 and IGS GIM are depicted in Fig. 9. The investigated time moment refers to 13:55 UT on 1 July 2008. VTEC differences up to 9 TECU between IRI-2007 and IGS GIM appear in Fig. 9 (right panel) along the geomagnetic equator and the northeastern region although the time corresponds to quiet conditions outside of solar and local noon maxima. Both areas are a part of the border of the crest region that is moving westwards. In Fig. 10, the absolute VTEC computed with our model, estimated Δ VTEC and the difference between the model estimation and IGS GIM are shown. In this scenario, a group of FORMOSAT-3/COSMIC (C2) profiles has been observed close to the depicted time moment and is located in the equatorial region, where significant differences between IRI-2007 and IGS GIM appear. The estimated Δ VTEC in Fig. 10 (middle panel) yields a decrease of up to 4.5 TECU with respect to the initial IRI-2007 model in the region correlated with the positions of the FORMOSAT-3/COSMIC profiles. A closer look at Fig. 10 (right panel) shows that the eye-catching discrepancy between IRI-2007 and IGS GIM is extensively reduced by the measurements and that our model solution closely resembles the IGS GIM data. Other regions that do not benefit from the impact of measurements are dominated by prior information. One needs to keep in mind that the prior information has been derived from IRI-2007, which means specifically that the difference between our model estimation and IGS GIM equals the difference between IRI-2007 and IGS GIM in regions without measurements. This becomes obvious when comparing Figs. 9 (right panel) and 10 (right panel), where, among other things, the difference in the northeastern part remains due to the lack of profiles.

5 Summary and conclusions

In this paper, the advantage of using electron density profiles that are able to describe the vertical electron density structure has been exploited for the determination of the physically defined F2 Chapman key parameters $NmF2$, $hmF2$ and $HF2$. As a mathematical distribution function, the concept of determining series coefficients for polynomial B splines with respect to longitude, latitude and time has been successfully applied. The adapted Chapman function is introduced as a relatively simple mathematical formulation that considers, although rudimentary, a plasmasphere extension.

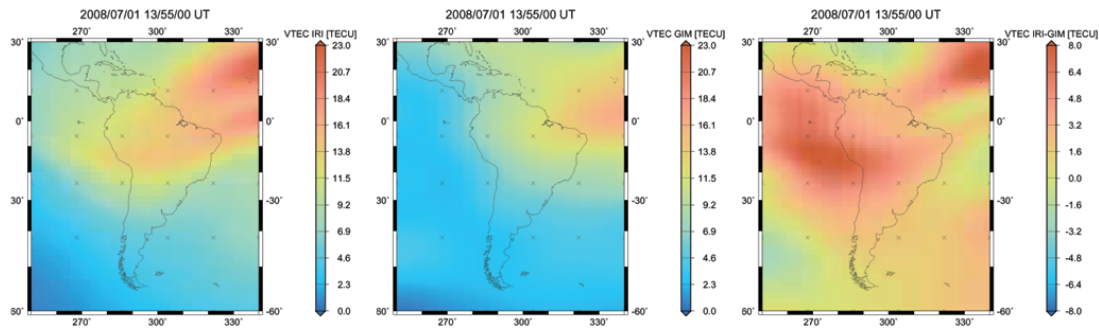


Fig. 9. VTEC maps referring to (left) IRI-2007, (middle) IGS GIM and (right) the difference between IRI-2007 and IGS GIM for 1 July 2008 at 13:55 UT (from left to right).

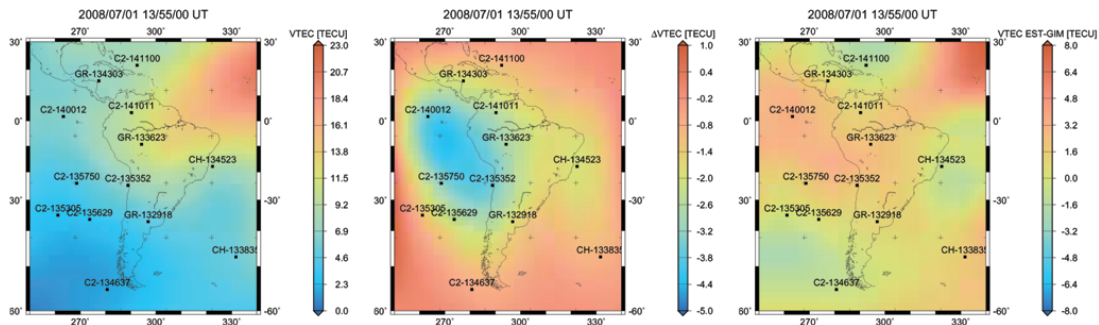


Fig. 10. VTEC maps referring to (left) the model estimation, (middle) estimated Δ VTEC and (right) the difference between the model estimation and IGS GIM for 1 July 2008 at 13:55 UT (from left to right).

E layer manifestations nevertheless cannot be intercepted by this model function, leading to mismodeling effects as soon as the E layer influence becomes prominent. Investigations on a more sophisticated model, including the consideration of lower atmospheric layers, are intended for upcoming studies. However, selected validation procedures on the basis of closed-loop simulations and profile evaluations with real data have demonstrated the functionality of the model. Although the results are based on a rather limited set of observations and short time frame during low solar activity, there is significant potential in the approach. Investigations on the estimated VTEC have been performed by comparisons with the climatological model IRI-2007 and the GNSS-driven VTEC solutions provided by the IGS. In general, the rather sparse distribution of electron density profiles considered as input observations results in few areas where the electron density parameters are adjusted. Corrections are computed at locations where profiles are available, and the results correspond well to the IGS GIMs, which demonstrates the potential of electron density profiles coupled with this model approach to improve existing solutions for appropriate key parameters. The determination system presented provides a basis for the combined usage of electron density profiles with other observation techniques to enable the mutual support concerning individual sensitivities with respect to different key parameters. Future work will include the combination of various

observation techniques. In particular, electron density profiles will be combined with ground- and space-based GNSS, DORIS and radar altimetry in order to benefit from the advantages of a higher spatio-temporal data resolution and the availability of measurements to bridge data gaps over the oceans.

Acknowledgements. The authors are very grateful to the ionospheric research group of the Institute of Communications and Navigation at DLR Neustrelitz for providing the preprocessed GRACE and CHAMP data and thank Lung-Chih Tsai from CSRSR at the NCU, Taiwan, for the FORMOSAT-3/COSMIC electron density profiles. Many thanks also go to Dieter Bilitza and one anonymous reviewer for the helpful comments. This work has been conducted as part of the project “Multi-scale model of the ionosphere from the combination of modern space-geodetic satellite techniques”, which is funded by the German Research Foundation (DFG), Bonn, Germany.

Topical Editor K. Hosokawa thanks D. Bilitza and one anonymous referee for their help in evaluating this paper.

References

- Aragon-Angel, A.: Contributions to ionospheric electron density retrieval, Ph.D. Thesis, Research Group of Astronomy and Geomatics (gAGE), Technical University of Catalonia (UPC), 53–63, 2010.
- Bilitza, D. and Reinisch, B.: International reference ionosphere 2007: Improvements and new parameters, *Adv. Space Res.*, 42, 599–609, doi:10.1016/j.asr.2007.07.048, 2008.
- Davies, K.: Ionospheric radio, Peter Peregrinus Ltd., London, 1990.
- Dettmering, D., Schmidt, M., Heinkelmann, R., and Seitz, M.: Combination of different space-geodetic observations for regional ionosphere modeling, *J. Geodesy*, 85, 989–998, doi:10.1007/s00190-010-0423-1, 2011a.
- Dettmering, D., Heinkelmann, R., and Schmidt, M.: Systematic differences between VTEC obtained by different space-geodetic techniques during CONT08, *J. Geodesy*, 85, 443–451, doi:10.1007/s00190-011-0473-z, 2011b.
- Dow, J. M., Neilan, R. E., and Rizos, C.: The International GNSS Service in a changing landscape of Global Navigation Satellite Systems, *J. Geodesy*, 83, 191–198, doi:10.1007/s00190-008-0300-3, 2009.
- Hajj, G. A. and Romans, J.: Ionospheric electron density profiles obtained with the Global Positioning System: Results from the GPS/MET experiment, *Radio Sci.*, 33, 175–190, doi:10.1029/97RS03183, 1998.
- Hernández-Pajares, M., Juan, J. M., and Sanz, J.: Improving the Abel inversion by adding ground data LEO radio occultations in the ionospheric sounding, *Geophys. Res. Lett.*, 27, 2743–2746, doi:10.1029/2000GL000032, 2000.
- Hernández-Pajares, M., Juan, J. M., Sanz, J., Orus, R., Garcia-Rigo, A., Feltens, J., Komjathy, A., Schaer, S. C., and Krankowski, A.: The IGS VTEC maps: a reliable source of ionospheric information since 1998, *J. Geodesy*, 83, 263–275, 2009.
- Hoque, M. M. and Jakowski, N.: A new global model for the ionospheric F2 peak height for radio wave propagation, *Ann. Geophys.*, 30, 797–809, doi:10.5194/angeo-30-797-2012, 2012.
- Jakowski, N.: Ionospheric GPS radio occultation measurements on board CHAMP, *GPS Solutions*, 9, 88–95, doi:10.1007/s10291-005-0137-7, 2005.
- Jakowski, N., Wehrenpfennig, A., Heise, S., Reigber, C., Lühr, H., Grunewaldt, L., and Meehan, T.: GPS radio occultation measurements of the ionosphere from CHAMP: Early results, *Geophys. Res. Lett.*, 29, doi:10.1029/2001GL014364, 2002.
- Jakowski, N., Leitinger, R., and Angling, M.: Radio occultation techniques for probing the ionosphere, *Ann. Geophys.*, 47, doi:10.4401/ag-3285, 2004.
- Jayachandran, B., Krishnankutty, T. N., and Gulyaeva, T. L.: Climatology of ionospheric slab thickness, *Ann. Geophys.*, 22, 25–33, doi:10.5194/angeo-22-25-2004, 2004.
- Kirchengast, G., Foelsche, U., and Steiner, A. K.: Occultations for probing atmosphere and climate, Springer Berlin Heidelberg, ISBN 3-540-22350-9, 2004.
- Koch, K. R.: Parameter estimation and hypothesis testing in linear models, Springer, Berlin, 1999.
- Koch, K.-R. and Kusche, J.: Regularization of geopotential determination from satellite data by variance components, *J. Geodesy*, 76, 259–268, doi:10.1007/s00190-002-0245-x, 2002.
- Lyche, T. and Schumaker, L. L.: A multiresolution tensor spline method for fitting functions on the sphere, *SIAM J. Sci. Comput.*, 22, 724–746, doi:10.1137/S1064827598344388, 2000.
- Reinisch, B. W., Nsumeia, P., Huang, X., and Bilitza, D. K.: Modeling the F2 topside and plasmasphere for IRI using IMAGE/RPI and ISIS data, *Adv. Space Res.*, 39, 731–738, doi:10.1016/j.asr.2006.05.032, 2007.
- Rishbeth, O. K. and Garriot, H.: Introduction to Ionospheric Physics, Academic Press, New York, 1969.
- Schmidt, M.: Wavelet modeling in support of IRI, *Adv. Space Res.*, 39, 932–940, doi:10.1016/j.asr.2006.09.030, 2007.
- Schmidt, M., Dettmering, D., Mößmer, M., Wang, Y., and Zhang, J.: Comparison of spherical harmonic and B spline models for vertical total electron content, *Radio Sci.*, 46, RS0D11, doi:10.1029/2010RS004609, 2011.
- Schumaker, L. L.: Spline functions basic theory, John Wiley and Sons Inc., New York, ISBN 0-471-76475-2, 1981.
- Tsai, L.-C. and Tsai, W.-H.: Improvement of GPS/MET ionospheric profiling and validation using the Chung-Li ionosonde measurements and the IRI model: Terrestrial, Atmospheric and Oceanic Sciences (TAO), 15, 589–607, doi:10.3319/TAO.2007.12.19.01(F3C), 2004.
- Tsai, L.-C., Liu, C. H., and Hsiao, T. Y.: Profiling of ionospheric electron density based on FormoSat-3/COSMIC data: results from the intense observation period experiment: Terrestrial, Atmospheric and Oceanic Sciences (TAO), 20, 181–191, 2009.
- Ware, R., Exner, M., Feng, D., Gorbunov, M., Hardy, K., Melbourne, W., Rocken, C., Schreiner, W., Sokolovsky, S., Solheim, F., Zou, X., Anthes, A. R., Businger, S., and Trenberth, K.: GPS Sounding of the Atmosphere from Low Earth Orbit: Preliminary Results, *B. Am. Meteorol. Soc.*, 77, 19–40, doi:10.1175/1520-0477(1996)077<0019:GSOTAF>2.0.CO;2, 1996.
- Wright, J. W.: A model of the F region above *hmF2*, *J. Geophys. Res.*, 65, 185–191, 1960.
- Zeilhofer, C., Schmidt, M., Bilitza, D., and Shum, C. K.: Regional 4-D modeling of the ionospheric electron density from satellite data and IRI, *Adv. Space Res.*, 43, 1669–1675, doi:10.1016/j.asr.2008.09.033, 2008.